JOURNAL OF GEOPHYSICAL RESEARCH, VOL. 106, NO. B12, PAGES 30,689–30,699, DECEMBER 10, 2001

Microearthquake seismicity and focal mechanisms at the Rodriguez Triple Junction in the Indian Ocean using ocean bottom seismometers

Kei Katsumata,[1] Toshinori Sato,[2] Junzo Kasahara,[3] Naoshi Hirata,[3] Ryota Hino,[4] Narumi Takahashi,[5] Mayumi Sekine,[6] Seiichi Miura,[5] Sadayuki Koresawa,[3] and Naoto Wada[1,7]

Abstract. Hypocenters and focal mechanisms of microearthquakes have been investigated at the Rodriguez Triple Junction in the Indian Ocean. Little was known on microearthquake activity in this region. We deployed 18 ocean bottom seismographs during the KH93-3 cruise of the R/V *Hakuho-Maru* (Ocean Research Institute, University of Tokyo) from July 30 to August 20, 1993. We obtained 579 well-constrained hypocenters and 13 focal mechanisms. Microearthquakes were found to be active along all of the three ridges: the Central Indian Ridge, the Southeastern Indian Ridge, and the Southwestern Indian Ridge. Especially at the triple junction there was an earthquake swarm within narrow area of approximately 15×5 km^2. All of the 13 focal mechanisms showed normal or strike-slip faultings, which means that the extensional stress field characterizes this region.

1. Introduction

The Indian Ocean triple junction, which is called the Rodriguez Triple Junction (RTJ), is a ridge-ridge-ridge (RRR) type triple junction located near 25.5°S, 70.0°E (Figure 1). Three spreading ridges make the Indo-Australia, the Antarctica, and the Africa plates. The Central Indian Ridge (CIR) and the Southeast Indian Ridge (SEIR) spread at intermediate speed (47.5 and 55.0 mm/yr), and Southwest Indian Ridge (SWIR) spreads at a very slow speed (13.6 mm/yr) [*DeMets et al.*, 1994].

The RTJ has generally evolved as a RRR-type triple junction for the last 10 m.y. [*Tapscott et al.*, 1980]. On timescales of 1 m.y., many investigators proposed complicated evolutionary processes of the RTJ on the basis of topographic, magnetic, and gravitational studies. *Munschy and Schlich* [1989] proposed an unstable ridge-ridge-transform fault (RRF) evolutionary model in which the CIR was progressively offset from the SEIR, with the triple junction being restored by small jumps. *Mitchell* [1991] considered that the present RTJ can be well explained as a RRR type with an asymmetric spreading of the CIR segment immediately north of the triple junction. *Honsho et al.* [1996] proposed a two-mode evolutionary model, one is a RRR-type continuous mode, the other is a discontinuous mode which includes a short-living propagation of the SEIR followed by rapid rifting of the SWIR and restoration of the CIR. They considered that these modes repeat several times.

The crustal structure beneath the RTJ was studied by *Funasaka et al.* [1995] and *Miura et al.* [1995] using ocean bottom seismometers (OBSs) with artificial sources. They noted that the oceanic layer 2 under the axis of the CIR is thinner than that under the axis of the SEIR. *Sato et al.* [1996] showed lateral heterogeneity of the crust and upper mantle beneath the RTJ using teleseismic travel time residuals. They revealed a relatively hotter mantle under the triple junction, along-axis variations at the SEIR segment, no hotter mantle under the SWIR segment, and an asymmetrical distribution of residuals at the CIR segment.

Seismicity provides basic and important data to the understanding of the present tectonics and evolutionary process of the RTJ. Because the RTJ is located far from lands, detectability and resolution of earthquakes are very poor by land-based observations. To reveal microseismicity at and around the RTJ, we conducted a 1-month seismic observation using 18 OBSs. In this paper, we present detailed microearthquake seismicity and focal mechanisms at and around the RTJ deduced from OBS data.

2. Data Acquisition

We deployed 18 OBSs during the KH93-3 cruise of the R/V *Hakuho-Maru* (Ocean Research Institute, University of Tokyo) in 1993 (Figure 2 and Table 1). The observation period was from July 30 to August 20 (~3 weeks). We obtained good quality data for the present study from 15 OBSs except OBS 2, 13, and 14. There were two types of OBS used in the cruise: Earthquake Research Institute (ERI) type developed at the Faculty of Science, the University of Tokyo [*Yamada et al.*, 1981; *Kasahara et al.*, 1985], and TK type developed by T. Kanazawa at the Department of Earth Sciences, Chiba University [*Matsuda et al.*, 1986; *Kanazawa and Shiobara*, 1994]. Nine OBSs (2, 3, 4, 10, 12, 14, 16, 17, and 18) were equipped with 2-Hz natural frequency velocity seismometers (one verti-

[1]Institute of Seismology and Volcanology, Hokkaido University, Sapporo, Japan.
[2]Graduate School of Science, Chiba University, Chiba, Japan.
[3]Earthquake Research Institute, University of Tokyo, Tokyo, Japan.
[4]Graduate School of Science, Tohoku University, Sendai, Japan.
[5]Japan Marine Science and Technology Center, Yokosuka, Japan.
[6]Association for the Development of Earthquake Prediction, Tokyo, Japan.
[7]Now at Shibetsu-cho Town Office, Shibetsu, Japan.

Paper number 2000JB000106.
0148-0227/01/2000JB000106$09.00

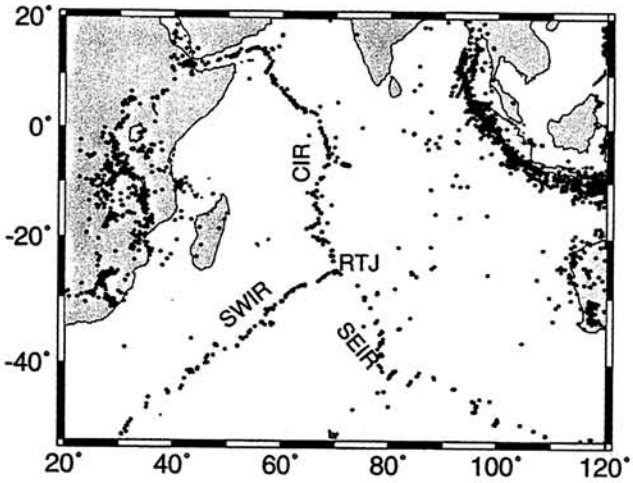

Figure 1. Three mid-oceanic ridges and the Rodriguez Triple Junction (RTJ). CIR, Central Indian Ridge; SWIR, Southwestern Indian Ridge; and SEIR: Southeastern Indian Ridge. Dots are epicenters with $M = 5.0$ and larger located by International Seismology Center from 1971 to 1990.

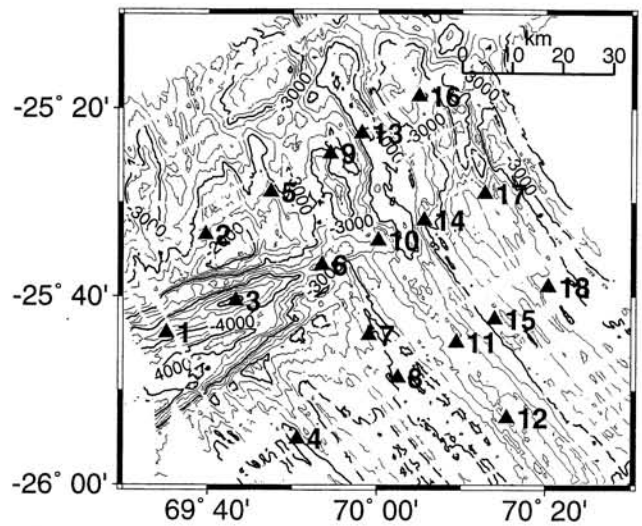

Figure 2. Distribution of OBSs (triangles) in the RTJ. Contours show a topography of ocean bottom with an interval of 250 m. The bathymetric data were obtained during the Rodriguez II cruise by the R/V *Jean Charcot* [*Munschy and Schlich*, 1989] and the KH93-3 cruise by the R/V *Hakuho-Maru*.

cal and one horizontal) and a hydrophone [*Kasahara et al.*, 1979]. The other nine OBSs (1, 5, 6, 7, 8, 9, 11, 13, and 15) had 4.5-Hz natural frequency velocity seismometers (one vertical and two horizontal). Each OBS used a quartz clock with a typical precision of 10^{-7}, and an analog recording system provided a direct continuous recording on cassette tapes. We measured time differences between the quartz clock in OBS and the GPS clock on the ship at deployment and retrieval and calculated a time drift by linear interpolation.

During the observation period we also conducted seismic reflection and refraction experiments. We could take full advantage of a detailed topographic data previously acquired by SeaBeam [*Munschy and Schlich*, 1989] for design of the air gun shooting line and selection of the exact place for OBS deployment. Because we planned the experiment for both a controlled seismic experiment and observation of natural earthquakes, we distributed the OBSs at equal spacing of ~20 km, as shown in Figure 2. Exceptions are in the vicinity of the RTJ where the OBSs are located about every 10 km. Since little was known on microearthquake seismicity in this region before our observation, we deployed OBSs to cover the region as widely as possible. As a result, a depth of hypocenter was not well constrained, as shown in section 3.

Before deployment of each OBS we made a detailed topographic map at a scale of about 1:50,000 and chose a position with relatively smooth topography for the OBS site. As was shown by the 3.5-kHz profiling data, the seafloor is extremely rough and seemed to have no sediment. All OBS positions were examined using a detailed topographic map, which were

Table 1. Positions and Characteristics of OBSs

OBS	Institute[a]	Latitude S	Longitude E	Depth, m	Component[b]	Recording Systems[c]	Period
1	CHU	25°43.92′	69°35.07′	4538	V, H, H	A, C	July 29 to Aug. 16
2	ERI	25°33.40′	69°39.66′	2768	H, H, P	A, C	July 29 to Aug. 16
3	ERI	25°40.38′	69°43.15′	5065	V, H	A, C	July 29 to Aug. 19
4	ERI	25°55.16′	69°50.51′	3056	V, H	A, C	July 30 to Aug. 19
5	CHU	25°28.99′	69°47.28′	2543	V, H, H, P	A, C	July 29 to Aug. 16
6	THK	25°36.87′	69°53.49′	3975	V, H, H	A, C	July 29 to Aug. 19
7	THK	25°44.14′	69°59.08′	2927	V, H, H	A, C	July 30 to Aug. 19
8	THK	25°48.64′	70°02.53′	3115	V, H, H	A, C	July 30 to Aug. 20
9	CHU	25°24.83′	69°54.25′	2841	V, H, H, P	A, C	July 29 to Aug. 17
10	ERI	25°34.03′	69°59.58′	3404	V, H	A, C	July 29 to Aug. 19
11	THK	25°44.89′	70°09.42′	3658	V, H, H	A, C	July 30 to Aug. 20
12	ERI	25°50.54′	70°13.80′	3824	V, H, P	A, C	July 31 to Aug. 20
13	CHU	25°22.69′	69°58.09′	4202	V, H, H, P	A, C	July 29 to Aug. 18
14	ERI	25°32.05′	70°05.52′	3052	V, H, P	A, C	July 30, lost
15	THK	25°42.34′	70°14.04′	2876	V, H, H	A, C	July 30 to Aug. 20
16	ERI	25°18.93′	70°04.99′	2930	V, H, P	A, C	July 29 to Aug. 17
17	ERI	25°29.22′	70°12.58′	2294	V, H, P	A, C	July 30 to Aug. 18
18	ERI	25°38.94′	70°20.38′	2900	V, H, P	A, C	July 30 to Aug. 20

[a]CHU, Chiba University; ERI, Earthquake Research Institute, University of Tokyo; THK, Tohoku University.
[b]V, vertical geophone; H, horizontal geophone; P, hydrophone.
[c]A, analog; C, continuous.

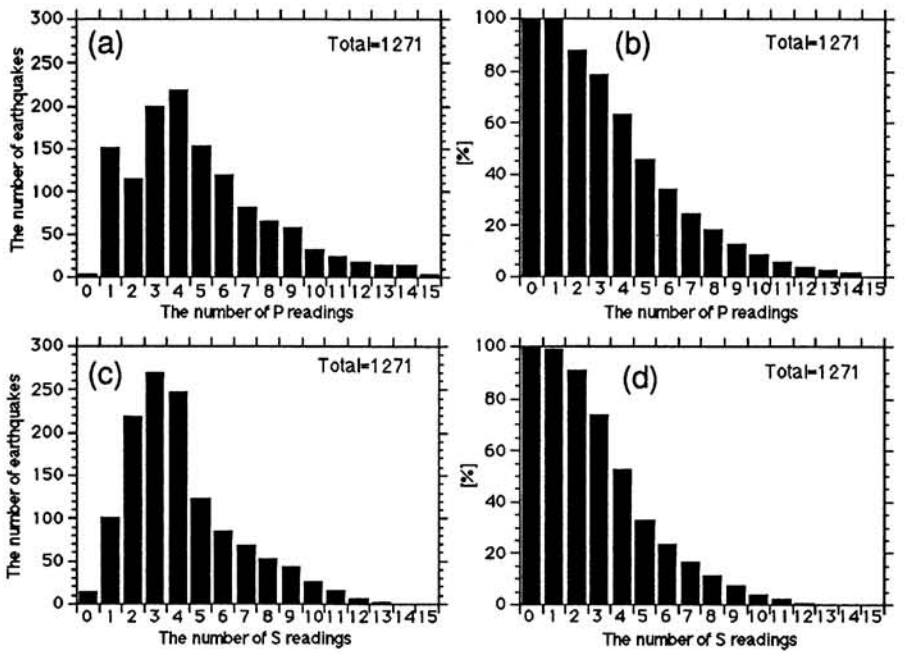

Figure 3. The number of readings of travel times for each earthquake. (a) and (c) Number of readings of *P* and *S* waves versus the number of earthquakes, respectively. (b) and (d) Decrease of earthquakes as the number of readings increases. For example in Figure 3b a column at four in the horizontal axis has a height of ~63%, which means that if you select events with four or more *P* wave arrival times, the number of the events corresponds to 63% of the total number of events detected.

made by the SeaBeam data acquired during the present cruise by the R/V *Hakuho-Maru*. We found a small discrepancy between the previous and the present SeaBeam topographic data depending on location in the surveyed area. In general, the difference is from 0.2 to 0.4 km. We shifted the scheduled position of the OBS deployment after acquisition of swath mapping data on board.

Positions of deployment for all OBSs are listed in Table 1, which are located by a GPS navigation on the R/V *Hakuho-Maru*. It took less than half an hour to complete deployment of the OBS after arriving at the scheduled position. We deployed the OBSs from the northeast OBS, 16, toward southwest. It took ~20 hours to complete the deployment for all the OBSs including transit between sites.

3. Method for Hypocentral Location

3.1. Earthquake Detection

All data recorded on the cassette tapes were converted from analog to digital data with sampling rates between 70 and 100 Hz. Events were detected at each seismic station using the ratio of STA/LTA. STA and LTA are short- and long-term averages of velocity amplitudes, respectively. We used 3.0 as the STA/LTA ratio and 64 s and 1 s as time windows for calculating LTA and STA. When more than two stations detected an event within 60 s, the event was interpreted as an earthquake, and the time was listed on a timetable for the next process. Waveforms of the detected earthquakes for all stations were cut out according to the timetable and then compiled into a data file with the WIN format [*Urabe and Tsukada*, 1992].

3.2. Arrival Time Data

The arrival times of *P* and *S* waves were picked manually from careful inspection of the vertical and horizontal seismograms using the WIN program [*Urabe and Tsukada*, 1992], which is a powerful tool for high-speed display of waveforms on an UNIX workstation, picking up arrival times of *P* and *S* waves and calculating a hypocenter. Figure 3 shows a summary of *P* and *S* waves readings. In the observation period, 1271 earthquakes were detected manually. Rather small earthquakes detected by only three or four OBSs were dominant (Figures 3a and 3c). Though we need lots of hypocenters to discuss seismicity, small earthquakes were not located well. Theoretically, four arrival times of *P* waves are able to give three parameters for position and an origin time. However, more than four data should be required because using more data with good quality decreases the estimation error in calculation of hypocenter. In this study we selected 583 earthquakes with five and more *P* wave arrival time data, which corresponded to 46% of the total earthquakes detected (Figure 3b). Figures 4 and 5 show examples of waveforms for *P* and *S* wave, respectively.

3.3. Preliminary Calculation of Hypocenters

3.3.1. One-dimensional velocity structure. To locate hypocenters accurately, velocity structure should be assumed appropriately. *Funasaka et al.* [1995] and *Miura et al.* [1995] constructed two-dimensional *P* wave velocity models based on the seismic refraction experiment in the area of this study. Their models were modified to one-dimensional structure. The *P* wave velocities were assumed to be 5.8 and 8.0 km/s for the upper layer and for the lower half-space, respectively. The sea

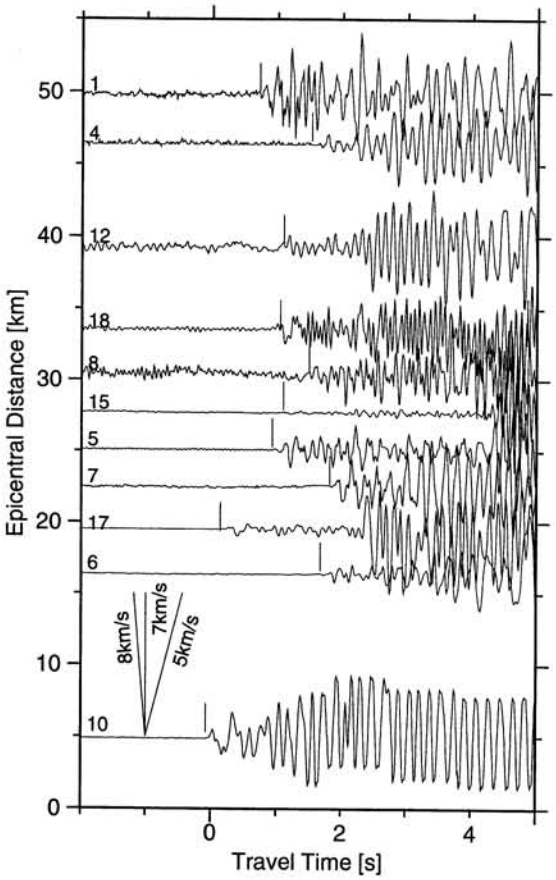

Figure 4. Example of waveforms of *P* wave recorded on vertical components. No correction has been made for the different instrument responses of the 2-Hz and 4.5-Hz OBSs. This earthquake occurred on August 6, 1993, with an epicenter at 25.5367°S, 70.0308°E. The horizontal axis indicates the reduced travel time measured from the origin time. The reduction velocity was 7.0 km/s. The OBS numbers shown in Figure 2 were labeled at the head of each trace. Vertical lines pointed to the onset of the *P* wave.

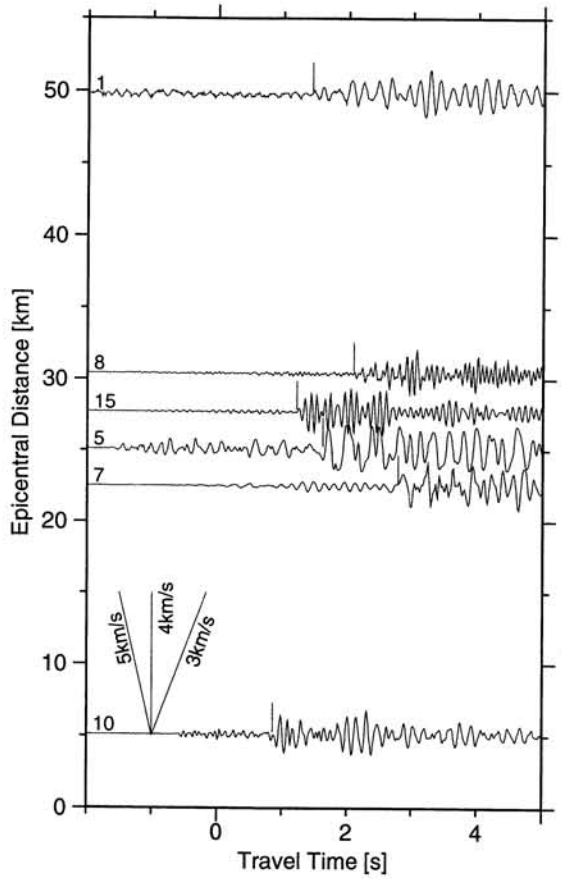

Figure 5. Example of waveforms of *S* wave recorded on horizontal components. This is the same earthquake as shown in Figure 4. The reduction velocity was 4.0 km/s. Vertical lines pointed to the onset of the *S* wave.

surface corresponds to 0 km. The upper layer was 9 km thick including the seawater. Theoretical travel time was calculated on the assumption that a layer of the seawater was filled with a solid with a *P* wave velocity of 5.8 km/s and the OBSs were buried in the solid corresponding to the depth of seawater.

3.3.2. V_p/V_s ratio. We have estimated V_p/V_s, which is the ratio of the compressional to shear wave velocities, by using a diagram [*Wadati*, 1933] at each ridge segment (Figure 6). We selected earthquakes with five and more *S-P* time data, plotted them versus the arrival time of *P* wave, and calculated a slope of linear regression by least squares method. We found that taking the variance into account, the averaged V_p/V_s ratios were equal to $\sqrt{3}$. Therefore the V_p/V_s ratio was assumed to be $\sqrt{3}$; that is, the Poisson's ratio was assumed to be 0.25 in each layer.

3.3.3. Preliminary location of hypocenters. Hypocenters were calculated by using a computer software called HYPOMH [*Hirata and Matsu'ura*, 1987], which is based on a simple algorithm to find a maximum likelihood solution with the Bayesian approach. Longitude and latitude of the OBS with the fastest arrival time were given as the initial epicenter. The initial depth of hypocenter was fixed at 7 km for all earthquakes. Station correc-

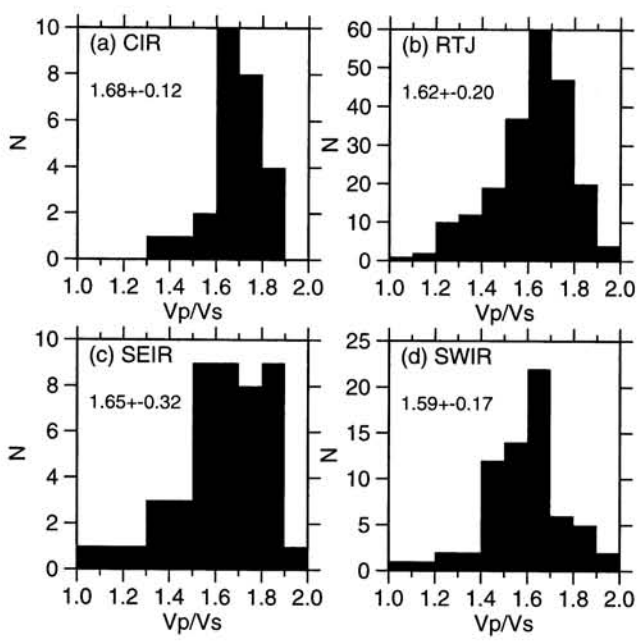

Figure 6. Histograms for V_p/V_s ratios. (a) Earthquakes on the CIR segment, (b) earthquakes in the active cluster near the triple junction, (c) earthquakes on the SEIR segment, and (d) earthquakes on the SWIR segment. Averaged V_p/V_s ratios and variances are indicated.

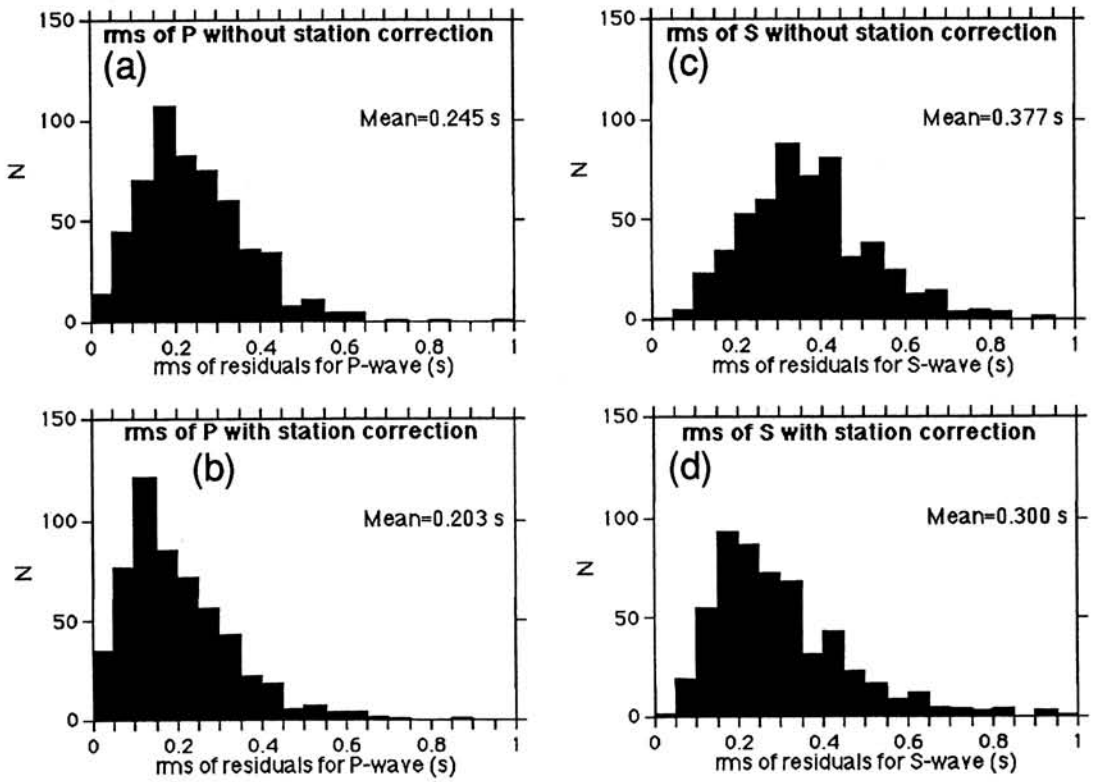

Figure 7. Histograms of the root mean squares of residuals of (a) and (b) P wave without and with station corrections, respectively. (c) and (d) S wave without and with station corrections, respectively.

tions were not applied. After the calculation the root-mean-square (RMS) of residuals for P and S waves peaked at 0.15–0.20 s and 0.30–0.35 s, respectively (Figures 7a and 7c).

3.4. Relocation of Hypocenters With Station Correction

3.4.1. Hypocenters. We estimated station corrections for each subregion and for each OBS as follows. First, the study area was divided into four subregions: CIR (25.18–25.43°S, 69.85–70.06°E), SWIR (25.53–26.00°S, 69.25–70.0°E), SEIR (25.57–26.0°S, 70.00–70.50°E), and RTJ (25.43–25.57°S, 70.00–70.20°E). Second, residuals at each station were averaged for all earthquakes in each subregion. We applied these averaged residuals to each OBS as station correction for the second calculation. Therefore the station correction varied depending on which subregion a hypocenter was located in the preliminary calculation. Both residuals for P and S waves obviously decreased after the relocation. The residuals were peaked at 0.10–0.15 s and 0.15–0.20 s for P and S waves, respectively (Figures 7b and 7d).

3.4.2. Magnitude. We calculated a magnitude M using a duration time of ground motion T_d [*Tsumura*, 1967]:

$$M = -2.36 + 2.85 \log T_d, \quad (1)$$

where T_d is in seconds. T_f, when an event ends, was defined as a time when amplitudes decrease below noise level. T_d is defined as $T_f - T_p$, where T_p is an arrival time of P wave. We have estimated T_p and T_f by eye-ball inspection on vertical component and calculated a magnitude at each seismic station for an earthquake. These magnitudes were averaged to obtain M for the earthquake. If you have continuous waveform data, using the duration time has an advantage in that you are able to measure it even for a large event for which the maximum amplitude is out of range. The disadvantage of this method is that T_d is dependent on the characteristics of the seismometer. In this study, this disadvantage caused no serious problem because we focused on only the relative size of earthquakes, which was required to determine the b values mentioned in section 3.5.

3.5. Location Error

We have conducted a simulation to estimate a location error as follows. Suppose that you choose an earthquake with arrival times of P wave at OBSs 1, 2, 3, and 4, and those of S wave at OBSs 1, 2, 3, and 4, and those of S wave were calculated for OBSs 2 and 4. The same P and S wave velocity structure mentioned in the section 3.3 was assumed to calculate theoretical travel times corresponding to real readings. In this case, theoretical travel times of P wave were calculated for OBSs 2 and 4. The hypocenter was assumed to be at the point obtained from the relocation with station corrections. Then we added random noises to the travel times. The noises were within ±10% of each travel time calculated, which was supposed to simulate discrepancies between the assumed one-dimensional velocity structure and the real one, and reading errors caused by a ground noise. For example, if a theoretical P wave travel time is 10 s at OBS 1, a noise within ±1 s is added, and if it is 5 s at OBS 2, a noise within ±0.5 s is added. The amount of noise varies as a function of travel times for each OBS. Then we assumed the same velocity structure in the section 3.3 and calculated a hypocenter by using these travel times. The procedure, that is, adding random noises to theoretical travel times and calculating a hypocenter, was repeated 500 times for the earthquake. The locations of the 500 hypocenters were averaged to obtain the mean latitude, longitude, and depth of

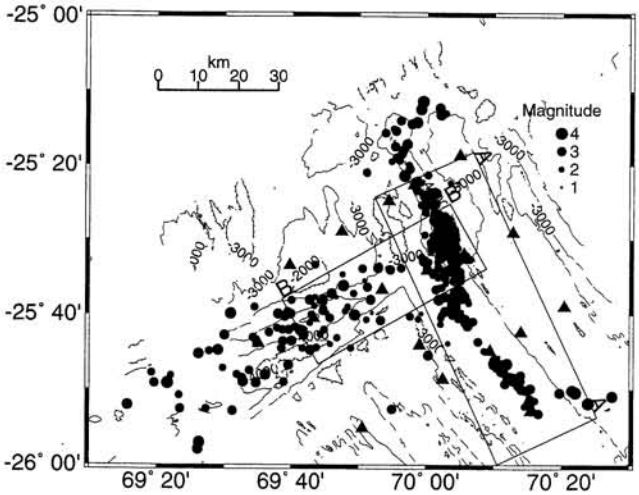

Figure 8. Epicenters of earthquakes at the Rodriguez Triple Junction in the Indian Ocean from July 30 to August 20 in 1993. Contours show a topography of ocean bottom with an interval of 1000 m. Two boxes labeled as AA′ and BB′ are regions for cross sections in Figure 10.

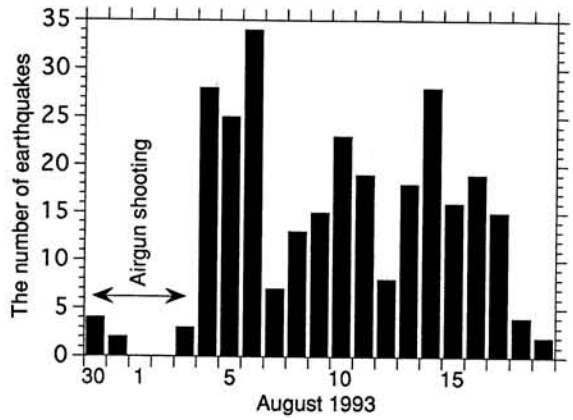

Figure 9. Number of hypocenters located in each day at the Rodriguez Triple Junction in the Indian Ocean.

the hypocenter. The standard deviations were also calculated, defined as the location error for the earthquake.

We have calculated the location errors for all earthquakes relocated in section 3.4 and found that in the horizontal direction, 70% of all earthquakes has a location error smaller than ±3 km, 20% has an error between ±3 and ±10 km, and 10% has an error larger than ±10 km. In the depth direction, only 10% of all earthquakes has a location error smaller than ±3 km, 60% has an error between ±3 and ±10 km, and 30% has an error larger than ±10 km.

4. Hypocentral Distribution

4.1. Epicenters

We obtained 579 relocated hypocenters in the study area. All these epicenters are shown in Figure 8, and some outstanding features of spatial pattern of seismicity were found: (1) Almost all earthquakes were located along the three ridges: CIR, SEIR, and SWIR. (2) Along the CIR and the SEIR, seismicity was limited in rather narrow zones. (3) Along the SWIR, earthquakes occurred over a broad area, not in a limited zone as along the CIR and the SEIR. The area including earthquakes seemed to correspond to the area with water depth deeper than 3500 m. (4) At the RTJ, there was an active cluster in which ~50% of the total number of earthquakes was located. The area of the cluster was approximately 15 × 5 km^2. A side with a length of 15 km seemed to be parallel to ridge axes of the CIR and the SEIR.

4.2. Seismicity Rates

Since OBSs were deployed in almost the same spacing, the detection capability should be almost same in the network. Thus we calculated a seismicity rate along each ridge and compared them with each other. A time period used for the calculation was between August 4 and August 17 for 2 weeks (Figure 9). In case of the SEIR, 67 hypocenters were located in the time period, and the length of seismic area was 35 km. Therefore the seismicity rate per kilometer was 50 events/yr. In case of CIR, 26 hypocenters were located, the length was 25 km long, and the rate was thus 27 events/yr. In case of the SWIR, 87 hypocenters were located, the length was 75 km long, and the rate was thus 30 events/yr. In the active cluster at the RTJ, there were 267 events in the time period. Thus the seismicity rate per kilometer along a direction of the 15 km side was 464 events per year. Since the observation period was very short, the difference among SEIR, CIR, and SWIR was not significant, while the active cluster at RTJ was noteworthy.

4.3. Depth of Hypocenters

We selected hypocenters with the location error estimated in section 3.5 as less than ±3 km in depth to plot on cross sections (Figure 10). Even though the earthquakes has relatively small location error, some hypocenters were plotted above a sea

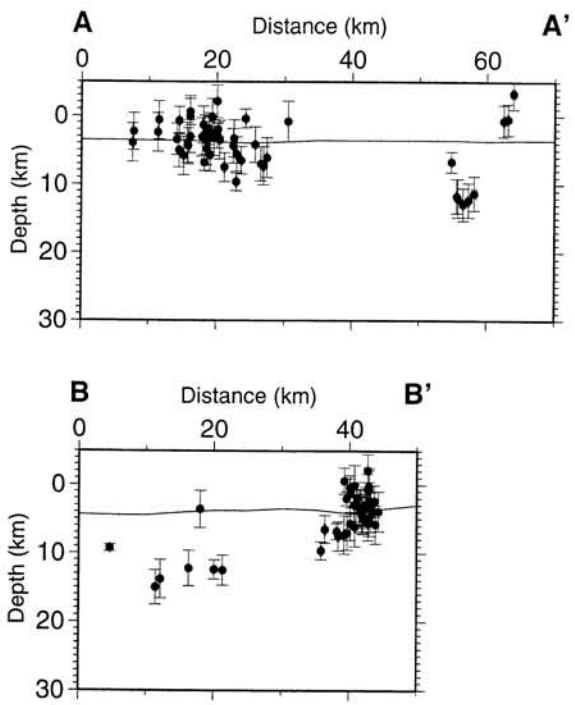

Figure 10. Cross sections for two regions labeled as AA′ and BB′ in Figure 8. Horizontal axis:vertical axis ratio is 1:1. Sea surface is 0 km in depth. Horizontal lines at a depth of around 4 km show the sea bottom.

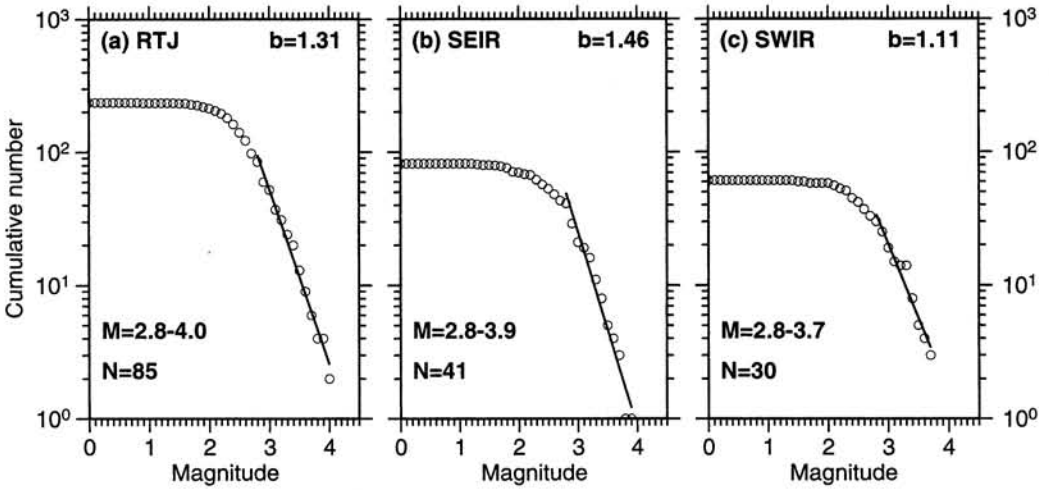

Figure 11. The b values for (a) the RTJ, (b) the SEIR, and (c) the SWIR. Earthquakes with $M = 2.8$ and larger were used.

bottom, which possibly means that they occurred at so shallow a crust that our seismic network was not able to constrain the depth. The active cluster at RTJ was plotted on section AA′ at a distance of around 20 km and on section BB′ at a distance of around 40 km. The focal depth of these events appeared to be concentrated at a portion shallower than 10 km, while on the other hand, there were deeper events at distances of 60 km on AA′ section and 20 km on BB′ section. If earthquakes deeper than 10 km occur at RTJ, we are able to locate them since the station coverage is the best in this network. However, the uncertainty of location due to sparse deployment of OBSs was too large to discuss a more detailed lateral change in depth.

4.4. The b Values

The frequency-magnitude distribution [*Ishimoto and Iida*, 1939; *Gutenberg and Richter*, 1944] describes the power law relation between the frequency of occurrence and magnitude of earthquake:

$$\log_{10}N = a - bM, \tag{2}$$

where N is the cumulative number of earthquakes having magnitude larger than M and a and b are constants. The b value in (2) can be perturbed for various reasons. The factors that result in high b values are as follow: (1) increased material heterogeneity or crack density [*Mogi*, 1962], (2) an increase in the thermal gradient [*Warren and Latham*, 1970]. On the other hand, low b values are caused by an increase in shear or effective stress [*Scholz*, 1968; *Urbanic et al.*, 1992; *Wyss*, 1973]. The b value decreases with depth in strike-slip fault zone [*Mori and Abercrombie*, 1997; *Wiemer and McNutt*, 1997], possibly because of the increased applied stress at greater depth. High b values ($b > 1.3$) are observed in creeping sections of faults [*Amelung and King*, 1997; *Wiemer and Wyss*, 1997], whereas asperities exhibit a low b value ($b < 0.6$) [*Wiemer and Wyss*, 1997]. The areas of largest slip release during the main shock correlate well with high b value regions in the aftershock zone [*Wiemer and Katsumata*, 1999]. In volcanic areas, high b values are observed near magma chambers and highly cracked volumes [*Wiemer and McNutt*, 1997; *Wyss et al.*, 1997; *Wiemer et al.*, 1998].

We calculated b values for the active cluster at the triple junction and earthquakes along the SEIR and the SWIR (Figure 11). The earthquakes along the CIR were too few to obtain the reliable b value. Linear regression gave $b = 1.31$ for the active cluster at RTJ, $b = 1.46$ for the SEIR, and $b = 1.11$ for the SWIR. The b values seemed to be different from each other. In order to evaluate the significance we estimated the probability that two samples may come from the same population by test [*Utsu*, 1992]:

$$P \approx \exp(-dA/2 - 2), \tag{3}$$

where $dA = -2N \ln(N) + 2N_1 \ln(N_1 + N_2 b_1/b_2) + 2N2 \ln(N_1 b_2/b_1 + N_2) - 2$ and $N = N_1 + N_2$. In the case of comparing SEIR and SWIR, $b_1 = 1.46$, $N_1 = 41$, $b_2 = 1.11$, and $N_2 = 30$, and thus $P = 0.19$. Comparing RTJ and SWIR, $b_1 = 1.31$ and $b_2 = 1.46$, and thus $P = 0.31$. The probabilities are not considerably small. Therefore in the statistical meaning, we cannot prove the difference between each region. However, we speculate that the SWIR produces earthquakes with smaller b value than produced by the RTJ and the SEIR; this might be related to the small spreading rate.

5. Focal Mechanisms

Normal faulting characterizes focal mechanisms on segments of mid-ocean ridges [e.g., *Sykes*, 1967]. Many previous studies were based on teleseismic waveform data revealing the focal mechanisms of rather large events. On the other hand, few studies have researched focal mechanisms of microearthquakes because of the difficulty in deploying enough number of OBSs to determine the focal mechanisms by plotting first motions of P wave. Composite fault plane solutions for inner floor events at the Mid-Atlantic Ridge near 23°N indicated normal faulting on planes dipping at angles near 45° [*Toomey et al.*, 1988]. Six focal mechanisms obtained from P wave first motions for events within the transform valley of the Kane Transform Fault indicated a tension axis perpendicular to the trend of the transform [*Wilcock et al.*, 1990]. At the segment of the Mid-Atlantic Ridge axis near 26°N, fault plane solutions indicate normal faultings beneath the along-axis high and the base of the adjacent western wall [*Kong et al.*, 1992]. At 29°N on the Mid-Atlantic Ridge a composite solution also showed normal

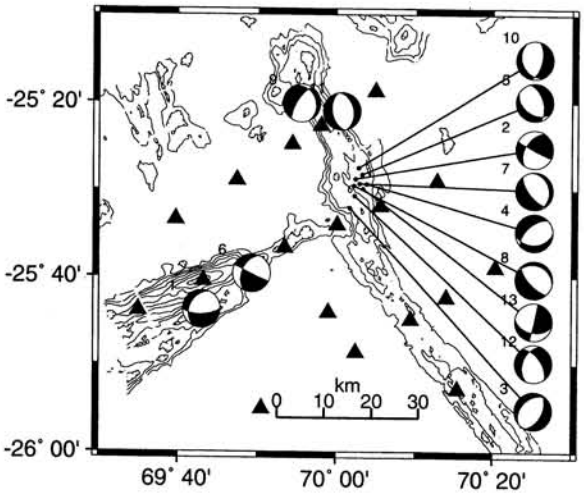

Figure 12. Focal mechanisms determined from *P* wave first motions. Lower hemisphere projection was used. Shadowed areas represent compressional *P* wave first arrivals. The numbers attached to each mechanism are the event numbers as shown in Figure A1. Contours show a topography of ocean bottom with a water depth of 3500 m and deeper. Solid triangles are OBSs.

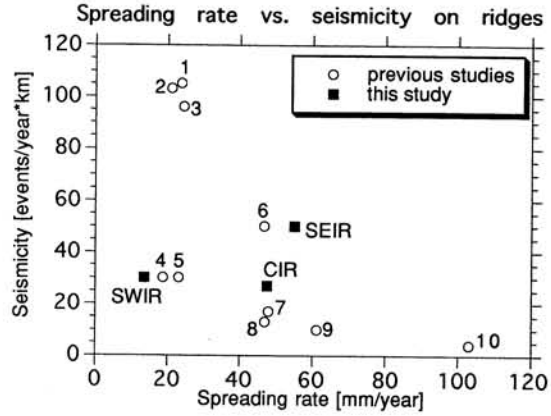

Figure 14. Spreading rate versus microearthquake seismicity on axes of mid-oceanic ridges. Open circles denote results from previous studies: 1, *Kong et al.* [1992]; 2, *Lilwall and Kirk* [1985]; 3, *Toomey et al.* [1988]; 4, *Watanabe et al.* [1992]; 5, *Wolfe et al.* [1995]; 6, *Sohn et al.* [1998a]; 7, *Hildebrand et al.* [1997]; 8, *Sohn et al.* [1998b]; 9, *Riedesel et al.* [1982]; 10, *Wilcock et al.* [1992]. Solid squares show the results from our study: the Southeast Indian Ridge (SEIR), the Central Indian Ridge (CIR), and the Southwest Indian Ridge (SWIR). Ocean bottom spreading rates were calculated by NUVEL-1A [*DeMets et al.*, 1994].

faulting [*Wolfe et al.*, 1995]. At the south end of the CoAxial segment of the Juan de Fuca Ridge, normal faulting on ridge-parallel, high-angle (80°) faults generated the posteruption earthquake activity [*Sohn et al.*, 1998a]. Not only the *P* wave polarities but also the empirically corrected ratios of *P* and *S* waves amplitudes were used to determine focal mechanisms. Using this method, *Shen et al.* [1997] found that intraplate microearthquakes had a variety of focal mechanisms on the west flank of the southern East Pacific Rise.

In this study, focal mechanisms were determined by plotting first motions of *P* wave with assumption of double couple. We selected well-recorded earthquakes having six and more first motion data with sharp onset. Nodal planes were manually drawn with eye-ball inspection. We obtained 13 well-constrained focal mechanisms in the study area (Figure 12). All the mechanisms showed normal or strike-slip faults. Nine of 13 earthquakes occurred in the active cluster at the RTJ, two along the SWIR, and two along the CIR. No focal mechanism was determined along the SEIR. We interpreted that the extensional stress field characterizes this region because the normal faultings were dominant. This fact is consistent with a model that the mid-ocean ridges are spreading centers of ocean bottom. The directions of tensional axes of the focal mechanisms were found to be also consistent with the model (Figure 13). The direction of tensional axes of events along the CIR and the SWIR was very close to that of ocean floor spreading predicted by the NUVEL-1A [*DeMets et al.*, 1994]. Seven of nine events at the RTJ had tensional axes striking the same direction as the spreading of the CIR or the SEIR. However, there were two exceptions.

6. Discussions

Low seismicity rate are typical of fast spreading ridges, whereas high seismicity rates are typical of slow spreading ridges. Figure 14 shows spreading rates versus seismicity rates along various mid-ocean ridges in the world. Seismicity along

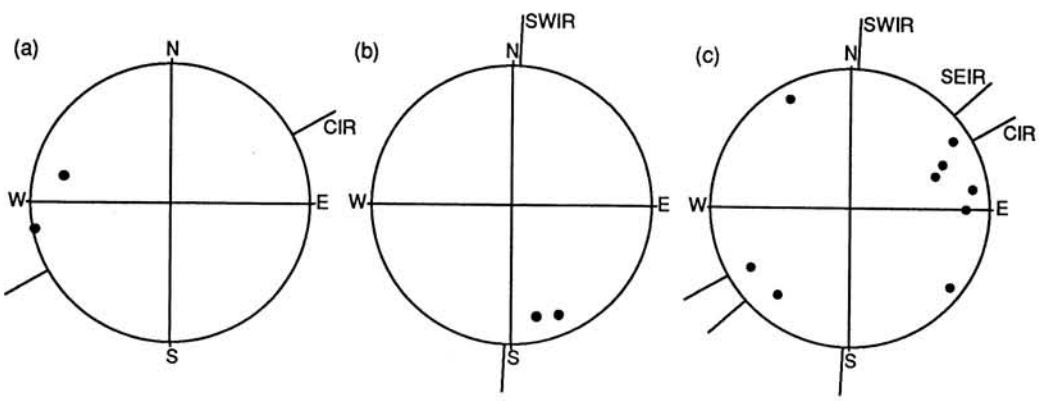

Figure 13. Summary of *T* axes for (a) the CIR, (b) the SWIR, and (c) the RTJ and comparison with the directions of ocean floor spreading.

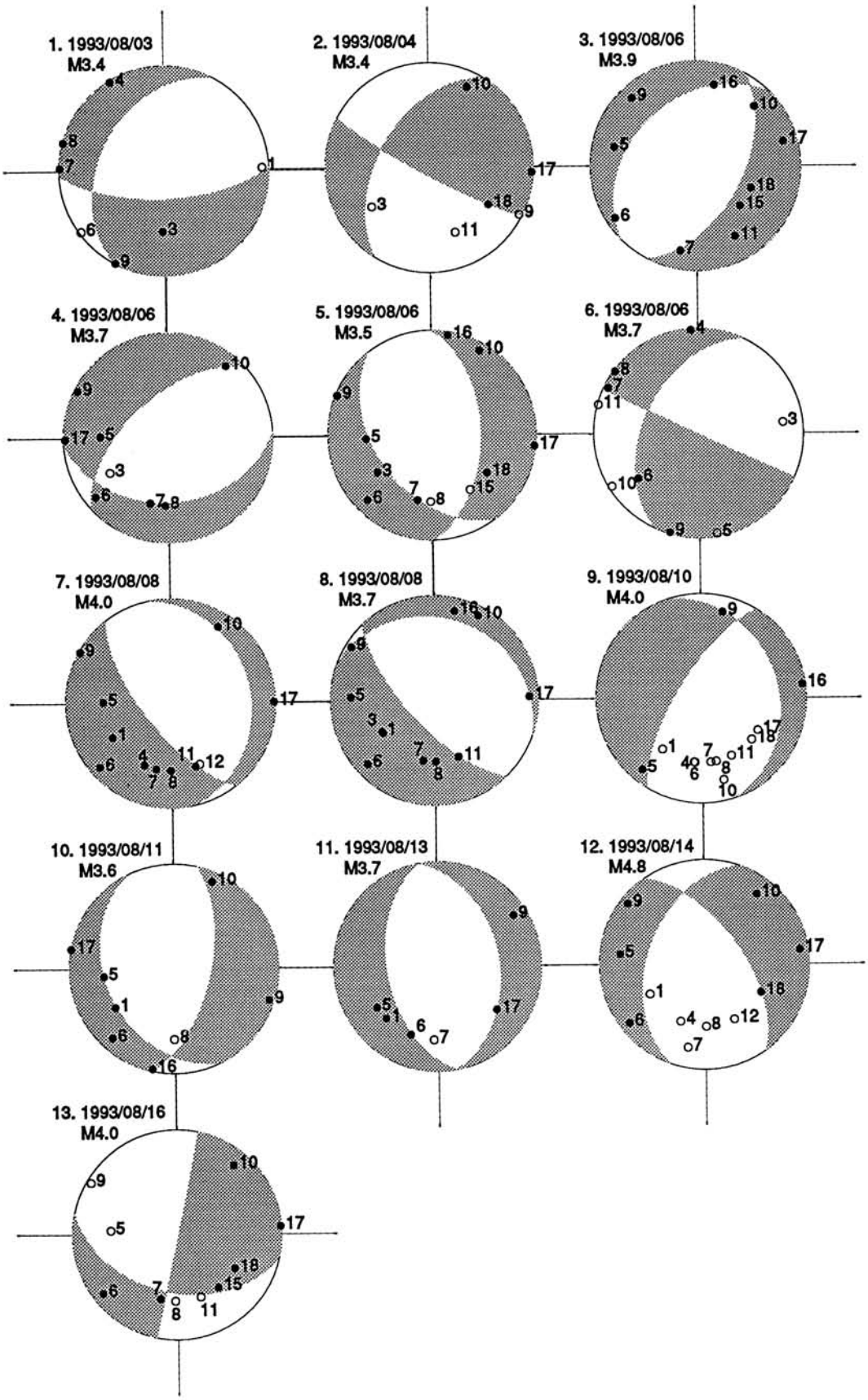

Figure A1. Focal mechanisms determined by plotting first motions of *P* wave with assumption of double couple. All diagrams are equal-area projections of the lower hemisphere of the focal sphere. Solid and open circles with OBS number indicate compressions and dilatations, respectively.

transform faults was not considered. The relation is not a simple inverse proportion: seismicity rates are ranging widely even for the same spreading rate. The maximum seismicity rate likely depends on a rate of ocean floor spreading.

A study on the relative travel time residuals of teleseismic events reveals that the CIR, the SEIR, and the SWIR have different characteristics [*Sato et al.*, 1996]. They suggested that there is a relatively hotter mantle beneath the triple junction and the northern part of the SEIR segment, along-axis variations in mantle temperature along the SEIR segment, and cooler mantle beneath the SWIR segment. In this study we found that the bottoms of seismogenic layer were relatively deep beneath the SWIR segment and relatively shallow beneath the triple junction. These two facts agree with the suggestion of *Sato et al.* [1996]. On the other hand, the bottom was almost same beneath the northern part of the SEIR segment as beneath the SWIR segment. This suggests that the mantle beneath the SEIR segment is as cool as that beneath the SWIR segment. Travel time delay observed in the northern part of the SEIR segment by *Sato et al.* [1996] could be explained if the crustal thickness was assumed to be larger. Negative Bouguer anomaly was observed also in the northern part of the SEIR by *Honsho et al.* [1996], which they interpreted to represent upwelling of the hot mantle along the ridge axes. However, change in the crustal thickness could reduce the anomaly to some extent. More careful research for the Moho depth should be required beneath this segment.

7. Conclusions

In this study we clearly found the following facts: (1) Microearthquake activities exist along all of three ridges: the CIR, the SEIR, and the SWIR. (2) Rates of occurrence of earthquakes were 27, 30, and 50 events yr^{-1} km^{-1} for the CIR, the SWIR, and the SEIR, respectively. (3) The rate for the small area near the triple junction was extremely high: 464 events yr^{-1} km^{-1}. (4) Spatial pattern of epicenters had outstanding features: epicenters were located in the narrow zones along the CIR and the SEIR, whereas along the SWIR, epicenters were spreaded out in the broad area.

Appendix A: Focal Mechanisms

Thirteen focal mechanisms were determined in this study. The polarity data and its distribution showed how well nodal planes were constrained (Figure A1).

Acknowledgments. We thank S. C. Solomon and an anonymous reviewer for instructive comments. We also thank the officers and crew of the R/V *Hakuho-Maru* and the scientist party of the KH93-3 research cruise for their help in collecting data. GMT system [*Wessel and Smith*, 1991; *Smith and Wessel*, 1990] was used to process and map data. This work was supported by a grant in aid (05302021) from the Ministry of Education, Science, Sports and Culture of Japan.

References

Amelung, F., and G. King, Earthquake scaling laws for creeping and non-creeping faults, *Geophys. Res. Lett.*, *24*, 507–510, 1997.

DeMets, C., R. G. Gordon, D. F. Argus, and S. Stein, Effect of recent revisions to the geomagnetic reversal time scale on estimates of current plate motions, *Geophys. Res. Lett.*, *21*, 2191–2194, 1994.

Funasaka, J., R. Hino, N. Hirata, J. Kasahara, T. Sato, and C. Igarashi, Seismic crustal structure in the Indian Ocean (Rodriguez) Triple Junction area, part 3, Upper crustal structure around the Southeast/Southwest/Central Indian Ridge, paper presented at Japan Earth and Planetary Science Joint Meeting, Tokyo, 1995.

Gutenberg, R., and C. F. Richter, Frequency of earthquakes in California, *Bull. Seismol. Soc. Am.*, *34*, 185–188, 1944.

Hildebrand, J. A., M. A. McDonald, and S. C. Webb, Microearthquakes at intermediate spreading-rate ridges: The Cleft segment megaplume site on the Juan de Fuca Ridge, *Bull. Seismol. Soc. Am.*, *87*, 684–691, 1997.

Hirata, N., and M. Matsu'ura, Maximum-likelihood estimation of hypocenter with origin time eliminated using nonlinear inversion technique, *Phys. Earth Planet. Inter.*, *47*, 50–61, 1987.

Honsho, C., K. Tamaki, and H. Fujimoto, Three-dimensional magnetic and gravity studies of the Rodriguez Triple Junction in the Indian Ocean, *J. Geophys. Res.*, *101*, 15,837–15,848, 1996.

Ishimoto, M., and K. Iida, Observations of earthquakes registered with the microseismograph constructed recently, *Bull. Earthquake Res. Inst. Univ. Tokyo*, *17*, 443–478, 1939.

Kanazawa, T., and H. Shiobara, Newly developed ocean-bottom seismometer, paper presented at Japan Earth and Planetary Science Joint Meeting, Sendai, Japan, 1994.

Kasahara, J., S. Koresawa, S. Nagumo, T. Daikuhara, T. Hara, and S. Ando, Free fall pop-up OBS (ERI type p-79), *Bull. Earthquake Res. Inst. Univ. Tokyo*, *54*, 515–530, 1979.

Kasahara, J., M. Takahashi, T. Matsubara, and M. Komiya, Mass storage digital ocean bottom seismometer and hydrophone (DOBSH) controlled by micro-processors using ADPCM voice synthesizing, *Bull. Earthquake Res. Inst. Univ. Tokyo*, *60*, 23–27, 1985.

Kong, L., S. Solomon, and G. M. Purdy, Microearthquake characteristics of a mid-ocean ridge along-axis high, *J. Geophys. Res.*, *97*, 1659–1685, 1992.

Lilwall, R. C., and R. E. Kirk, Ocean-bottom seismograph observations on the Charlie-Gibbs fracture zone, *Geophys. J. R. Astron. Soc.*, *80*, 195–208, 1985.

Matsuda, N., T. Fujii, and H. Kinoshita, Pop-up ocean bottom seismometer with hydrophone (in Japanese), *Abstr. Seismol. Soc. Jpn.*, no. 2, 241, 1986.

Mitchell, N. C., Distributed extension at the Indian Ocean triple junction, *J. Geophys. Res.*, *96*, 8019–8043, 1991.

Miura, S., R. Hino, T. Sato, J. Kasahara, C. Igarashi, M. Shinohara, and N. Hirata, Seismic crustal structure in the Rodriguez Triple Junction area—Heterogeneity of upper crustal structure (in Japanese), paper presented at Japan Earth and Planetary Science Joint Meeting, Tokyo, 1995.

Mogi, K., Magnitude-frequency relation for elastic shocks accompanying fractures of various materials and some related problems in earthquakes, *Bull. Earthquake Res. Inst. Univ. Tokyo*, *40*, 831–853, 1962.

Mori, J., and R. E. Abercrombie, Depth dependence of earthquake frequency-magnitude distributions in California: Implications for the rupture initiation, *J. Geophys. Res.*, *102*, 15,081–15,090, 1997.

Munschy, M., and R. Schlich, The Rodriguez Triple Junction (Indian Ocean): Structure and evolution for the past one million years, *Mar. Geophys. Res.*, *11*, 1–14, 1989.

Riedesel, M., J. A. Orcutt, K. C. Macdonald, and J. S. McClain, Microearthquakes in the black smoker hydrothermal field, East Pacific Rise at 21°N, *J. Geophys. Res.*, *87*, 10,613–10,623, 1982.

Sato, T., K. Katsumata, J. Kasahara, N. Hirata, R. Hino, N. Takahashi, M. Sekine, S. Miura, and S. Koresawa, Travel-time residuals of teleseismic *P*-waves at the Rodriguez Triple Junction in the Indian Ocean using ocean-bottom seismometers, *Geophys. Res. Lett.*, *23*, 713–716, 1996.

Scholz, C. H., The frequency-magnitude relation of microfracturing in rock and its relation to earthquakes, *Bull. Seismol. Soc. Am.*, *58*, 399–415, 1968.

Shen, Y., D. W. Forsyth, J. Conder, and L. M. Dorman, Investigation of microearthquake activity following an intraplate teleseismic swarm on the west flank of the southern East Pacific Rise, *J. Geophys. Res.*, *102*, 459–475, 1997.

Smith, W. H. F., and P. Wessel, Gridding with continuous curvature splines in tension, *Geophysics*, *55*, 293–305, 1990.

Sohn, R. A., J. A. Hildebrand, and S. C. Webb, Postrifting seismicity and a model for the 1993 diking event on the CoAxial segment, Juan de Fuca Ridge, *J. Geophys. Res.*, *103*, 9867–9877, 1998a.

Sohn, R. A., D. J. Fornari, K. L. Von Damm, J. A. Hildebrand, and S. C. Webb, Seismic and hydrothermal evidence for a cracking event

on the East Pacific Rise crest at 9°50'N, *Nature*, *396*, 159–161, 1998b.

Sykes, L. R., Mechanism of earthquakes and nature of faulting on the mid-oceanic ridges, *J. Geophys. Res.*, *72*, 2131–2153, 1967.

Tapscott, C. R., P. Patriat, R. L. Fisher, J. G. Sclater, H. Hoskins, and B. Parsons, The Indian Ocean triple junction, *J. Geophys. Res.*, *85*, 4723–4739, 1980.

Toomey, D. R., S. C. Solomon, and G. M. Purdy, Microearthquakes beneath median valley of Mid-Atlantic Ridge near 23°N: Tomography and tectonics, *J. Geophys. Res.*, *93*, 9093–9112, 1988.

Tsumura, K., Determination of earthquake magnitude from total duration of oscillation, *Bull. Earthquake Res. Inst. Univ. Tokyo*, *45*, 7–18, 1967.

Urabe, T., and S. Tsukada, WIN—A workstation program for processing waveform data from microearthquake networks, paper presented at Fall Meeting, Seismol. Soc. of Jpn., Tsukuba, 1992.

Urbanic, T. I., C. I. Trifu, J. M. Long, and R. P. Toung, Space-time correlations of *b* values with stress release, *Pure Appl. Geophys.*, *139*, 449–462, 1992.

Utsu, T., On seismicity, in *Report of the Joint Research Institute for Statistical Mathematics*, pp. 139–157, Inst. for Stat. Math., Tokyo, 1992.

Wadati, K., On the travel time of earthquake waves, II, *Geophys. Mag.*, *7*, 101–111, 1933.

Warren, N. W., and G. V. Latham, An experimental study of thermally induced microfracturing and its relation to volcanic seismicity, *J. Geophys. Res.*, *75*, 4455–4464, 1970.

Watanabe, T., S. Kodaira, H. Shiobara, T. Kanazawa, R. Stefansson, G. B. Gudmundsson, and H. Shimamura, Microseismicity in the Reykjanes Ridge, July, 1990: hypocenter distribution derived from an OBS array (in Japanese), *J. Seismol. Soc. Jpn.*, *45*, 327–337, 1992.

Wessel, P., and W. H. F. Smith, Free software helps map and display data, *Eos Trans. AGU*, *72*, 441, 445–446, 1991.

Wiemer, S., and K. Katsumata, Spatial variability of seismicity parameters in aftershock zones, *J. Geophys. Res.*, *104*, 13,135–13,151, 1999.

Wiemer, S., and S. McNutt, Variations in frequency-magnitude distribution with depth in two volcanic areas: Mount St. Helens, Washington, and Mt. Spurr, Alaska, *Geophys. Res. Lett.*, *24*, 189–192, 1997.

Wiemer, S., and M. Wyss, Mapping the frequency-magnitude distribution in asperities: An improved technique to calculate recurrence time?, *J. Geophys. Res.*, *102*, 15,115–15,128, 1997.

Wiemer, S., S. R. McNutt, and M. Wyss, Temporal and three-dimensional spatial analysis of the frequency-magnitude distribution near Long Valley Caldera, California, *Geophys. J. Int.*, *134*, 409–421, 1998.

Wilcock, W. S. D., G. M. Purdy, and S. C. Solomon, Microearthquake evidence for extension across the Kane Transform Fault, *J. Geophys. Res.*, *95*, 15,439–15,462, 1990.

Wilcock, W. S. D., G. M. Purdy, S. C. Solomon, D. L. DuBois, and D. R. Toomey, Microearthquakes on and near the East Pacific Rise, 9°–10°N, *Geophys. Res. Lett.*, *19*, 2131–2134, 1992.

Wolfe, C. J., G. M. Purdy, D. R. Toomey, and S. C. Solomon, Microearthquake characteristics and crustal velocity structure at 29°N on the Mid-Atlantic Ridge: The architecture of a slow spreading segment, *J. Geophys. Res.*, *100*, 24,449–24,472, 1995.

Wyss, M., Towards a physical understanding of the earthquake frequency distribution, *Geophys. J. R. Astron. Soc.*, *31*, 341–359, 1973.

Wyss, M., K. Shimazaki, and S. Wiemer, Mapping active magma chambers by *b* value beneath Off-Izu volcano, Japan, *J. Geophys. Res.*, *102*, 20,413–20,433, 1997.

Yamada, T., A. Asada, and H. Shimamura, A pop-up ocean bottom seismograph (in Japanese), *Abstr. Seismol. Soc. Jpn.*, no. 2, 126, 1981.

R. Hino, Graduate School of Science, Tohoku University, Sendai 980-8578, Japan.

N. Hirata, J. Kasahara, and S. Koresawa, Earthquake Research Institute, University of Tokyo, Tokyo 113-0032, Japan. (hirata@eri.u-tokyo.ac.jp, kasa2@eri.u-tokyo.ac.jp)

K. Katsumata, Institute of Seismology and Volcanology, Hokkaido University, Sapporo 060-0810, Japan. (katsu@eos.hokudai.ac.jp)

S. Miura and N. Takahashi, Japan Marine Science and Technology Center, Yokosuka 237-0061, Japan. (narumi@euler.jamstec.go.jp)

T. Sato, Graduate School of Science, Chiba University, Chiba 263-8522, Japan. (satot@earth.s.chiba-u.ac.jp)

M. Sekine, Association for the Development of Earthquake Prediction, Tokyo 101-0064, Japan. (sekine@erc.adep.or.jp)

N. Wada, Shibetsu-cho Town Office, Shibetsu 086-1632, Japan.

(Received December 14, 2000; revised August 18, 2001;
accepted August 22, 2001.)